Controlling graphene plasmons with resonant metal antennas and spatial conductivity patterns

P. Alonso-González,[1] A. Y. Nikitin,[1,2] F. Golmar,[1,3] A. Centeno,[4] A. Pesquera,[4] S. Vélez,[1] J. Chen,[1] G. Navickaite,[5] F. Koppens,[5] A. Zurutuza,[4] F. Casanova,[1,2] L. E. Hueso,[1,2] R. Hillenbrand[2,6]*

[1]CIC nanoGUNE, 20018 Donostia-San Sebastián, Spain. [2]IKERBASQUE, Basque Foundation for Science, 48011 Bilbao, Spain. [3]I.N.T.I.-CONICET and ECyT-UNSAM, San Martín, Buenos Aires, Argentina. [4]Graphenea SA, 20018 Donostia-San Sebastián, Spain. [5]ICFO-Institut de Ciéncies Fotoniques, Mediterranean Technology Park, 08860 Casteldefells, Barcelona, Spain. [6]CIC nanoGUNE and UPV/EHU, 20018 Donostia-San Sebastián, Spain.

*Corresponding author. E-mail: r.hillenbrand@nanogune.eu

Graphene plasmons promise unique possibilities for controlling light in nanoscale devices and for merging optics with electronics. Here we introduce a versatile platform technology based on resonant optical antennas and conductivity patterns for launching and controlling of propagating graphene plasmons, constituting an essential step for the development of graphene plasmonic circuits. We demonstrate the launching and focusing of infrared graphene plasmons with geometrically tailored antennas, and how they refract when passing through a 2-dimensional conductivity pattern, here a prism-shaped bilayer. To that end, we directly map the graphene plasmon wavefronts using an imaging method that will also benefit the testing of future design concepts for nanoscale graphene plasmonic circuits and devices.

Surface plasmon polaritons (SPPs)—coupled excitations of photons and mobile charge carriers—in metals and doped semiconductors offer intriguing opportunities to control light in nanoscale devices (1–7). Plasmons provide both a strong local field enhancement and confinement, accompanied by an appreciable reduction of the wavelength compared to free-space radiation. However, plasmons in metals exhibit relatively strong losses and cannot be controlled by electrical fields. Consequently, a strong quest for novel plasmonic materials arises (8). Among them, doped graphene excels due to its two-dimensional nature and high carrier mobility, supporting plasmons with an extreme confinement and a wavelength that can be strongly reduced compared to photons of the same frequency (9–14). More importantly, the carrier concentration in graphene can be tuned by electrical gating, opening exciting avenues for nanoscale electrical control of light (15–21). The ultra-short graphene plasmon (GP) wavelengths, however, come at the expense of a large momentum mismatch with photonic modes of the same frequency (22–25). Future graphene plasmonic circuits (15) will thus critically depend on converting incident light into propagating GPs, and on controlling their propagation and focusing to enhance light-matter interactions.

Figure 1 introduces the launching of GPs with metal antennas. The calculations (26) consider gold rods of length L acting as resonant dipole antennas. As shown in Fig. 1A, they provide strong near fields of opposite polarity at the rod extremities. For the fixed illumination wavelength $\lambda_0 = 10.20$ μm, the near-field intensity enhancement factor $f^2 = (E/E_0)^2$

indicates the fundamental dipolar antenna resonance at $L = 2.9$ μm. E is the electric field averaged over the antenna surface and E_0 the incident electric field. The Fourier transform (FT) of Fig. 1A reveals antenna near fields with orders of magnitude increased momentum compared to the incident wavevector k_0 (Fig. 1C). When such antenna is placed on graphene (assuming a Fermi energy $E_F = 0.44$ eV and a carrier mobility μ = 1136 cm^2/(V·s)), the high-momentum near-field components match the GP wavevector, thus exciting propagating GPs. Indeed, we observe an oscillating near-field distribution around the antenna on graphene (Fig. 1D). The distance between the field maxima of same polarity (same color) yields the GP wavelength, $\lambda_p = 380$ nm, which is a factor of 27 smaller than λ_0 (24, 25). Accordingly, the FT of Fig. 1D yields a bright ring of diameter $k_p = 2\pi/\lambda_p = 27k_0$, corroborating propagating GPs (Fig. 1F). As expected, the excitation of GPs broadens and shifts the antenna resonance (black curve in Fig. 1E).

To analyze how efficient GPs are excited, we calculated the quantity $\eta_p = P_p/(I_0 A_{ant})$ (red curve in Fig. 1E), where P_p is the power transferred into graphene, I_0 the illuminating intensity and A_{ant} the geometrical antenna cross-section. η_p provides a good estimation for the cross-section exciting GPs relative to the antenna's geometrical cross-section (26). It clearly follows the antenna's resonance. Compared to non-resonant antennas, e.g., with a quadratic cross-section (600 × 600 nm), the efficiency on resonance is enhanced by a factor of 28. The resonant near-field enhancement around the antenna is thus the source for strong GP excitation.

Intriguingly, in Fig. 1D we observe plane GP wavefronts parallel to the antenna axis, in contrast to metal SPPs launched by dipole antennas (27). We explain these plane wavefronts by the weak diffraction of the GPs, resulting from their short wavelength compared to the antenna length. The antenna can be thus considered as an extended plasmon source with a length of several GP wavelengths.

For an experimental demonstration, we fabricated gold rods on CVD-grown graphene transferred onto a 5-nm-thick SiO$_2$ layer on a CaF$_2$ substrate (26). We imaged the near-field distribution with a scattering-type scanning near-field microscope (s-SNOM) using a dielectric Si tip (Fig. 2A). Tip and sample were illuminated with s-polarized light (electric field E_0) parallel to the antenna axis, thus efficiently exciting the antenna. While scanning the sample, the real part of the p-polarized tip-scattered light, Re($E_{s,p}$), is recorded simultaneously to topography (26). On metal plasmonic antennas, such imaging scheme yields the vertical near-field component, Re(E_z) (28). This scheme also allows for

mapping the vertical near field of the GPs wavefronts launched by the antenna. We stress the fundamental difference to former experiments (*24, 25*), where a metal tip was used to both excite and detect GPs, yielding complex images of plasmon interference.

Figure 2B shows the topography of two Au antennas on graphene being strongly off (left) and near resonance (right). Near-field images at $\lambda_0 = 11.06$ μm and $\lambda_0 = 10.20$ μm (Fig. 2, C and D) verify the dipolar mode on the right antenna. Importantly, we also observe short-range spatial near-field oscillations around this antenna. Their period is about 400 nm, matching the GP wavelength at mid-infrared frequencies (*24, 25*). Our experimental observations agree well with numerical simulations (Fig. 2, E and F) assuming $E_F = 0.44$ eV and $\mu = 1136$ cm^2/(Vs). These values, used in all the calculations throughout this work, are consistent with our former experiments, where similarly grown graphene was used (*24, 26*). Because of the relatively low mobility, the field oscillations decay within a few plasmon wavelengths. For quantitative comparison, we show in Fig. 2, G and H, the experimental and calculated near-field profiles, Re($E_{s,p}$) and Re(E_z), along the dashed black lines indicated in Fig. 2, C and D, and Fig. 2, E and F, respectively. We find an excellent agreement, particularly for the oscillation periods and relative field strengths.

Figure 2I depicts the plasmon wavelength λ_p extracted from near-field images taken at different illumination wavelengths λ_0. Good agreement with the calculations is found, confirming the GP origin of the near-field oscillations. Note that the experimental images directly reveal the plasmon wavefronts and wavelength λ_p (the later given by the distance between two consecutive field maxima of the same polarity (color)), rather than LDOS maps and $\lambda_p/2$ as observed in refs. (*24, 25*).

We also fabricated and imaged much shorter antennas (left structure in Fig. 2, B to F) being strongly off-resonance with the incident wavelength. Owing to the weak field enhancement, we do not observe GPs around them (Fig. 2, C and D). For the same reason, some asperities remaining from the lithography process do not launch GPs. This result proves that GPs are launched by the resonant antenna near fields and not by the tip.

Resonant antennas can be simultaneously used for engineering the GP wavefronts, as we demonstrate in the following with concave and convex antenna extremities. While the convex extremity launches diverging GPs (Fig. 3, A to C, same data as shown in Fig. 2, A, C, and E), the concave extremity launches converging GPs (Fig. 3, D to F), yielding a focus at a distance of about 400 nm, recognized by the change of the wavefront curvature (illustrated by green lines in Fig. 3D).

The concave extremity represents a 2D lens for focusing GPs (Fig. 3G). The focal length *f* is determined by the cavity radius, which nominally is 400 nm, and thus agrees well with the focus position observed in Fig. 3E. To analyze the focus, we plot in Fig. 3, H and I, the experimental and calculated near-field intensities, $|E_{s,p}|^2$ and $|E_z|^2$, along the white dashed lines in Fig. 3, E and F, respectively (red curves). The dashed lines trace the field at a constant distance of 400 nm around the antenna extremity. We observe a strongly localized intensity at the focus position (position 2 in Fig. 3, E and F), which is enhanced by a factor of about 6 compared to positions 1 and 3. Compared to the convex antenna extremity (grey curves in Fig. 3, H and I), the plasmon focus yields an about 3-fold enhanced intensity.

The GP focus is determined by the numerical aperture (NA) of the extremity and the GP wavelength, analogous to diffraction-limited optics. Generally, the full width at half maximum (FWHM) of a focus size at wavelength λ can be estimated by FWHM $\approx \lambda/(2\text{NA})$, where NA = sin($\alpha$). With $\alpha = 70°$ (from Fig. 3D) and $\lambda_p = 436$ nm, we calculate FWHM = 232 nm, agreeing well with FWHM = 235 nm in the experimental (Fig. 3H) and FWHM = 216 nm in the calculated (Fig. 3I) near-field profiles (red curves), respectively. Note that the focus size can be tailored by varying the NA. In Fig. 2C, where the opening angle α of the cavity and thus the numerical aperture are smaller ($\alpha = 29°$, NA = 0.485), we measure a larger FWHM = 458 nm (fig. S2), in agreement with the expected FWHM = 450 nm (*26*).

Both the launching of GPs with antennas and wavefront mapping offer unique possibilities for studying fundamental and applied aspects of graphene plasmonics. In Fig. 4 we demonstrate that the propagation direction of GPs can be controlled by 2D refractive elements based on spatial conductivity patterns, as recently proposed (*15*). Our experiment is illustrated in Fig. 4A. A resonant gold antenna is illuminated with field E_0 parallel to the antenna axis. The antenna fields launch GPs propagating perpendicular to the antenna, which are refracted at a prism structure where the Fermi energy and thus GP wavelength is locally modified.

In the experiment, the prism consists of a graphene bilayer (*26*), which is outlined by a dashed black line in the topography image (Fig. 4B). Its height is 0.8 nm (Fig. 4C). In the near-field image, Re($E_{s,p}$), we observe horizontal GP wavefronts above both the left-hand side and very end of the right-hand side of the antenna (wavelength $\lambda_{p,2}$), as before in Figs. 2 and 3. Inside the prism, we find an increased plasmon wavelength, $\lambda_{p,1} = 1.4\ \lambda_{p,2}$ (Fig. 4E). We explain it by a locally increased conductivity. Note that the conductivity, and thus the wavelength λ_p, scales with the Drude weight *D* (*29*). For stacks of decoupled graphene layers (where interlayer hopping of electrons is neglected), the Drude weight scales as $D \sim n_G^{1/2}l$ (*29*), with n_G being the carrier density per layer and *l* the number of layers. Assuming that the carriers are equally distributed between the layers (*30*), we obtain $n_G = n/l$, and subsequently $D \sim n^{1/2}l^{1/2}$, where *n* is the total carrier density equal to that of the monolayer graphene. For a bilayer the conductivity is thus 1.41 larger than in a monolayer, yielding $\lambda_{p,1}/\lambda_{p,2} = D = 1.41$, in agreement with our experimental finding.

Outside the left prism boundary, the wavefronts are tilted by 24°. For the propagation directions we find $\alpha_1 = 50°$ and $\alpha_2 = 26°$, yielding sin(α_1)/sin(α_2) = 1.75 (Fig. 4F). Our findings, $\lambda_{p,1}/\lambda_{p,2} > 1$ and sin(α_1)/sin(α_2) > 1, demonstrate that GPs qualitatively follow the most fundamental law of refraction, Snell's law:

$$\frac{\sin \alpha_1}{\sin \alpha_2} = \frac{n_2}{n_1} = \frac{\lambda_1}{\lambda_2} \quad (1)$$

In Fig. 4G we corroborate the GP refraction with a numerical calculation, assuming $E_{F,2} = 0.44$ eV for the graphene monolayer (as in Figs. 2 and 3). For the bilayer we increased the conductivity to match the experimental wavelength ratio, $\lambda_{p,1} = 1.4\lambda_p$ (Fig. 4H). We measure $\alpha_1 = 50°$ and $\alpha_2 = 30°$, yielding sin(α_1)/sin(α_2) = 1.53, qualitatively following Snell's law (Eq. 1). The quantitative discrepancy found in both experiment and theory, i.e., sin(α_1)/sin(α_2) > $\lambda_{p,1}/\lambda_{p,2}$, is attributed to the strong GP damping. In strongly absorbing media, Snell's law deviates from its simple form (Eq. 1), as fronts of constant amplitude and phase may exhibit different diffraction angles (*31*), which is not considered in our

analysis. While further studies are required for a better quantitative understanding, our results demonstrate that GP propagation can be controlled by refraction. In the future, local gating of graphene could open exciting avenues for electrically tunable refractive elements, among others for steering of GPs.

Launching and controlling of propagating GPs with resonant metal antennas and spatial conductivity patterns could lead to various applications, including GP focusing into gated graphene waveguides, resonators, modulators or plasmon interferometers for communication and sensing. By improved doping strategies and carrier mobility in graphene, we expect GPs to propagate over several wavelengths at mid-infrared, near-infrared, and telecommunication wavelengths. Resonant antenna devices might also be used for converting the GPs into far-field radiation, which would enable a purely optical read-out of graphene plasmonic circuits or wireless on-chip communication between them.

References and Notes

1. W. L. Barnes, A. Dereux, T. W. Ebbesen, Surface plasmon subwavelength optics. *Nature* **424**, 824–830 (2003). doi:10.1038/nature01937 Medline
2. S. A. Maier, *Plasmonics: Fundamentals and Applications* (Springer-Verlag, New York, 2007).
3. P. Mühlschlegel, H. J. Eisler, O. J. F. Martin, B. Hecht, D. W. Pohl, Resonant optical antennas. *Science* **308**, 1607–1609 (2005). doi:10.1126/science.1111886 Medline
4. S. I. Bozhevolnyi, V. S. Volkov, E. Devaux, J.-Y. Laluet, T. W. Ebbesen, Channel plasmon subwavelength waveguide components including interferometers and ring resonators. *Nature* **440**, 508–511 (2006). doi:10.1038/nature04594 Medline
5. F. López-Tejeira, S. G. Rodrigo, L. Martín-Moreno, F. J. García-Vidal, E. Devaux, T. W. Ebbesen, J. R. Krenn, I. P. Radko, S. I. Bozhevolnyi, M. U. González, J. C. Weeber, A. Dereux, Efficient unidirectional nanoslit couplers for surface plasmons. *Nat. Phys.* **3**, 324–328 (2007). doi:10.1038/nphys584
6. J. Lin, J. P. Mueller, Q. Wang, G. Yuan, N. Antoniou, X. C. Yuan, F. Capasso, Polarization-controlled tunable directional coupling of surface plasmon polaritons. *Science* **340**, 331–334 (2013). doi:10.1126/science.1233746 Medline
7. F. J. Rodríguez-Fortuño, G. Marino, P. Ginzburg, D. O'Connor, A. Martínez, G. A. Wurtz, A. V. Zayats, Near-field interference for the unidirectional excitation of electromagnetic guided modes. *Science* **340**, 328–330 (2013). doi:10.1126/science.1233739 Medline
8. A. Boltasseva, H. A. Atwater, Low-loss plasmonic metamaterials. *Science* **331**, 290–291 (2011). doi:10.1126/science.1198258 Medline
9. K. W. K. Shung, Dielectric function and plasmon structure of stage-1 intercalated graphite. *Phys. Rev. B* **34**, 979–993 (1986). doi:10.1103/PhysRevB.34.979
10. O. Vafek, Thermoplasma polariton within scaling theory of single-layer graphene. *Phys. Rev. Lett.* **97**, 266406 (2006). doi:10.1103/PhysRevLett.97.266406 Medline
11. G. W. Hanson, Dyadic Green's functions and guided surface waves for a surface conductivity model of graphene. *J. Appl. Phys.* **103**, 064302 (2008). doi:10.1063/1.2891452
12. M. Jablan, H. Buljan, M. Soljačić, Plasmonics in graphene at infrared frequencies. *Phys. Rev. B* **80**, 245435 (2009). doi:10.1103/PhysRevB.80.245435
13. B. Wunsch, T. Stauber, F. Sols, F. Guinea, Dynamical polarization of graphene at finite doping. *New J. Phys.* **8**, 318 (2006). doi:10.1088/1367-2630/8/12/318
14. M. Polini, R. Asgari, G. Borghi, Y. Barlas, T. Pereg-Barnea, A. MacDonald, Plasmons and the spectral function of graphene. *Phys. Rev. B* **77**, 081411 (2008). doi:10.1103/PhysRevB.77.081411
15. A. Vakil, N. Engheta, Transformation optics using graphene. *Science* **332**, 1291–1294 (2011). doi:10.1126/science.1202691 Medline
16. Z. Fang, Y. Wang, Z. Liu, A. Schlather, P. M. Ajayan, F. H. Koppens, P. Nordlander, N. J. Halas, Plasmon-induced doping of graphene. *ACS Nano* **6**, 10222–10228 (2012). doi:10.1021/nn304028b Medline

17. H. Yan, X. Li, B. Chandra, G. Tulevski, Y. Wu, M. Freitag, W. Zhu, P. Avouris, F. Xia, Tunable infrared plasmonic devices using graphene/insulator stacks. *Nat. Nanotechnol.* **7**, 330–334 (2012). doi:10.1038/nnano.2012.59
18. H. Yan, T. Low, W. Zhu, Y. Wu, M. Freitag, X. Li, F. Guinea, P. Avouris, F. Xia, Damping pathways of mid-infrared plasmons in graphene nanostructures. *Nat. Photonics* **7**, 394–399 (2013). doi:10.1038/nphoton.2013.57
19. L. Ju, B. Geng, J. Horng, C. Girit, M. Martin, Z. Hao, H. A. Bechtel, X. Liang, A. Zettl, Y. R. Shen, F. Wang, Graphene plasmonics for tunable terahertz metamaterials. *Nat. Nanotechnol.* **6**, 630–634 (2011). doi:10.1038/nnano.2011.146
20. A. N. Grigorenko, M. Polini, K. S. Novoselov, Graphene plasmonics. *Nat. Photonics* **6**, 749–758 (2012). doi:10.1038/nphoton.2012.262
21. F. J. García de Abajo, Graphene nanophotonics. *Science* **339**, 917–918 (2013). doi:10.1126/science.1231119 Medline
22. A. Y. Nikitin, F. Guinea, F. J. Garcia-Vidal, L. Martin-Moreno, Fields radiated by a nanoemitter in a graphene sheet. *Phys. Rev. B* **84**, 195446 (2011). doi:10.1103/PhysRevB.84.195446
23. F. H. L. Koppens, D. E. Chang, F. J. García de Abajo, Graphene plasmonics: A platform for strong light-matter interactions. *Nano Lett.* **11**, 3370–3377 (2011). doi:10.1021/nl201771h Medline
24. J. Chen, M. Badioli, P. Alonso-González, S. Thongrattanasiri, F. Huth, J. Osmond, M. Spasenović, A. Centeno, A. Pesquera, P. Godignon, A. Z. Elorza, N. Camara, F. J. García de Abajo, R. Hillenbrand, F. H. Koppens, Optical nano-imaging of gate-tunable graphene plasmons. *Nature* **487**, 77–81 (2012). Medline
25. Z. Fei, A. S. Rodin, G. O. Andreev, W. Bao, A. S. McLeod, M. Wagner, L. M. Zhang, Z. Zhao, M. Thiemens, G. Dominguez, M. M. Fogler, A. H. Castro Neto, C. N. Lau, F. Keilmann, D. N. Basov, Gate-tuning of graphene plasmons revealed by infrared nano-imaging. *Nature* **487**, 82–85 (2012). Medline
26. See supplementary materials on *Science* Online.
27. Y. Liu, S. Palomba, Y. Park, T. Zentgraf, X. Yin, X. Zhang, Compact magnetic antennas for directional excitation of surface plasmons. *Nano Lett.* **12**, 4853–4858 (2012). doi:10.1021/nl302339z Medline
28. M. Schnell, A. García-Etxarri, A. J. Huber, K. Crozier, J. Aizpurua, R. Hillenbrand, Controlling the near-field oscillations of loaded plasmonic nanoantennas. *Nat. Photonics* **3**, 287–291 (2009). doi:10.1038/nphoton.2009.46
29. H. Yan, X. Li, B. Chandra, G. Tulevski, Y. Wu, M. Freitag, W. Zhu, P. Avouris, F. Xia, Tunable infrared plasmonic devices using graphene/insulator stacks. *Nat. Nanotechnol.* **7**, 330–334 (2012). doi:10.1038/nnano.2012.59
30. Y.-M. Lin *et al.*, *Nano Lett.* **8**, 2120 (2008).
31. M. Born, E. Wolf, *Principles of Optics* (Pergamon, New York, 1959).
32. E. D. Palik, *Handbook of Optical Constants of Solids* (Academic Press, San Diego, CA, 1985).
33. E. H. Hwang, S. Das Sarma, Dielectric function, screening, and plasmons in two-dimensional graphene. *Phys. Rev. B* **75**, 205418 (2007). doi:10.1103/PhysRevB.75.205418
34. L. A. Falkovsky, Optical properties of graphene and IV-VI semiconductors. *Phys. Uspekhi* **51**, 887–897 (2008). doi:10.1070/PU2008v051n09ABEH006625
35. S. Ryu, L. Liu, S. Berciaud, Y. J. Yu, H. Liu, P. Kim, G. W. Flynn, L. E. Brus, Atmospheric oxygen binding and hole doping in deformed graphene on a SiO$_2$ substrate. *Nano Lett.* **10**, 4944–4951 (2010). doi:10.1021/nl1029607 Medline

Supplementary Materials
www.sciencemag.org/cgi/content/full/science.1253202/DC1
Materials and Methods
Figs. S1 and S2
References (*32–35*)
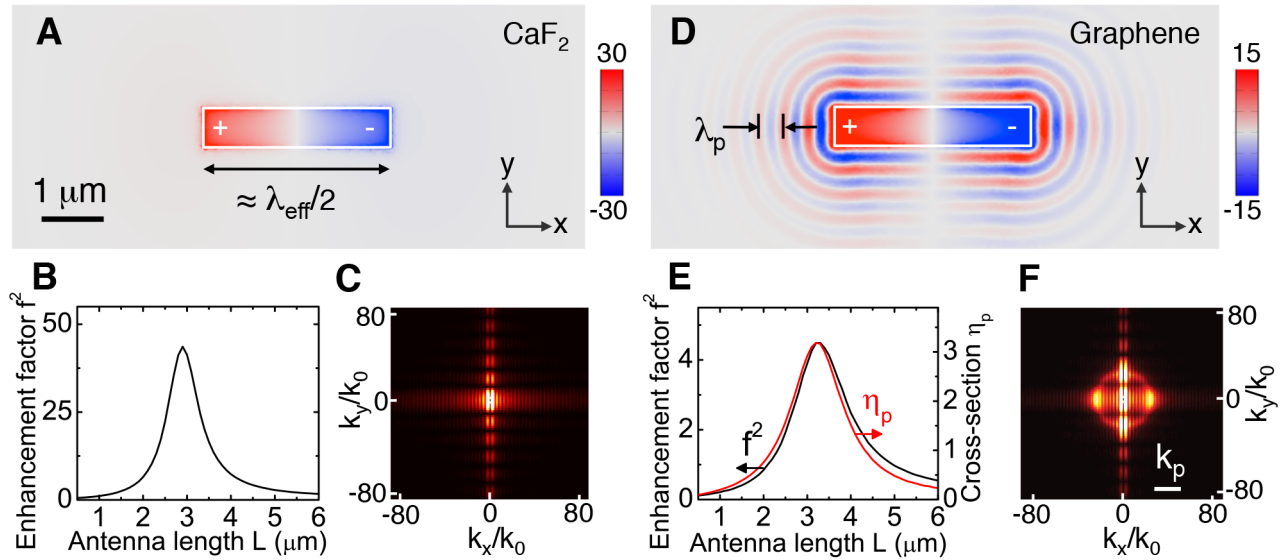
**Fig. 1. Numerical study of launching propagating GPs with resonant dipole antennas at $\lambda_0 = 10.20$ μm.**
(**A**) Near-field distribution of a resonant antenna (length $L = 2.9$ μm, width $w = 0.6$ μm and height $h = 40$ nm) on a CaF_2 substrate. (**B**) Near-field intensity enhancement factor f^2 as a function of L. (**C**) Absolute value of the Fourier transform of the near field in (A). (**D**) Near-field distribution of a resonant antenna ($L = 3.2$ μm, $w = 0.6$ μm, $h = 40$ nm) on graphene on a CaF_2 substrate. (**E**) Enhancement factor f^2 and η_p as a function of L. (**F**) Absolute value of the Fourier transform of the near field in (D). Panels (A) and (D) show the real part of the near-field z-component 5 nm above the antenna surface, normalized to $|E_0|$.
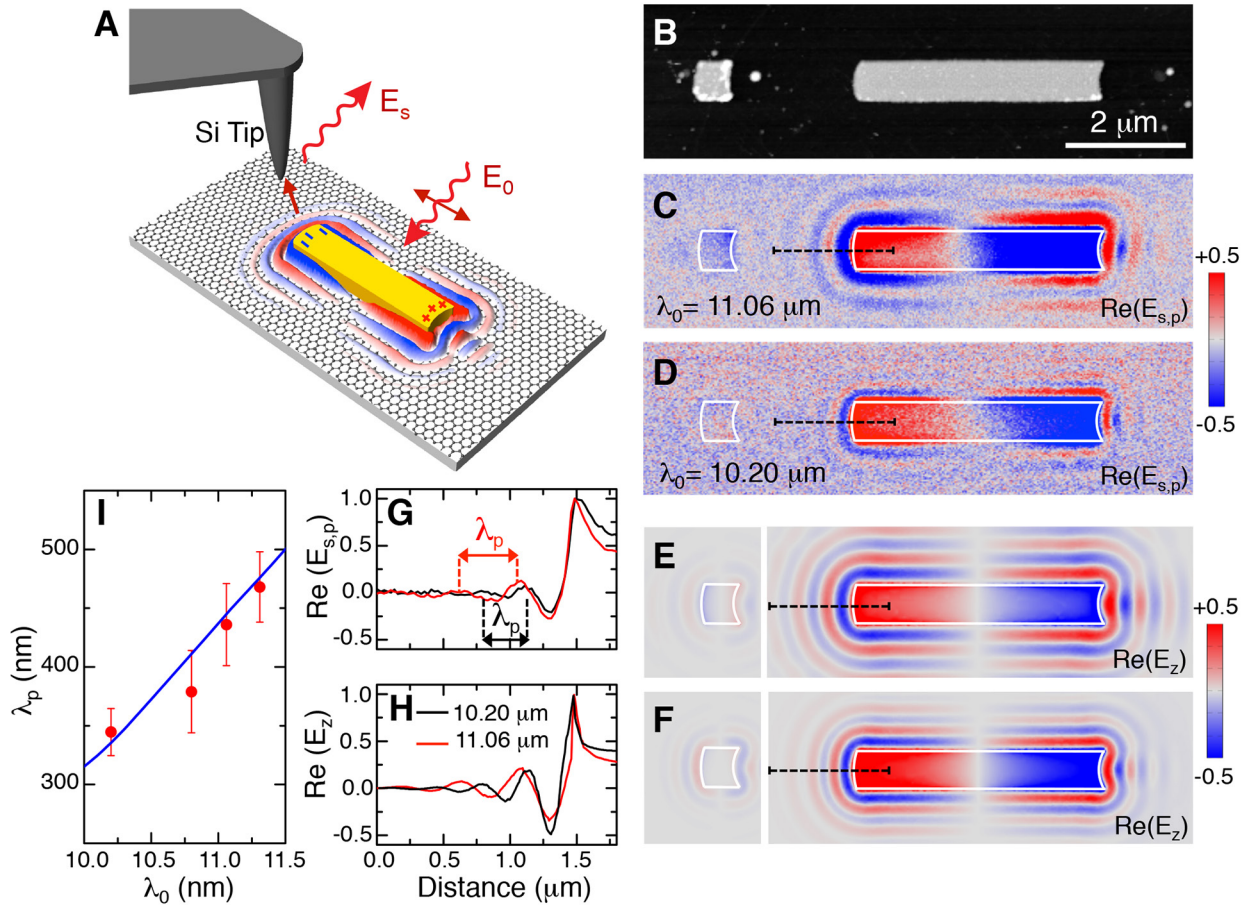
Fig. 2. Verification of an antenna-based GP launcher. (**A**) Illustration of the experiment. (**B**) Topography image of an off- and on-resonance dipole antenna (left and right, respectively). (**C** and **D**) Experimental and (**E** and **F**) calculated images, illustrating the real part of the vertical near-field component of the antennas shown in (B) for λ_0 = 11.06 μm and 10.20 μm, respectively. (**G**) Experimental and (**H**) calculated near-field profiles along the dashed black lines in (C, D) and (E, F), respectively. (**I**) Experimental (symbols) and calculated (solid line) GP wavelength λ_p as a function of λ_0.
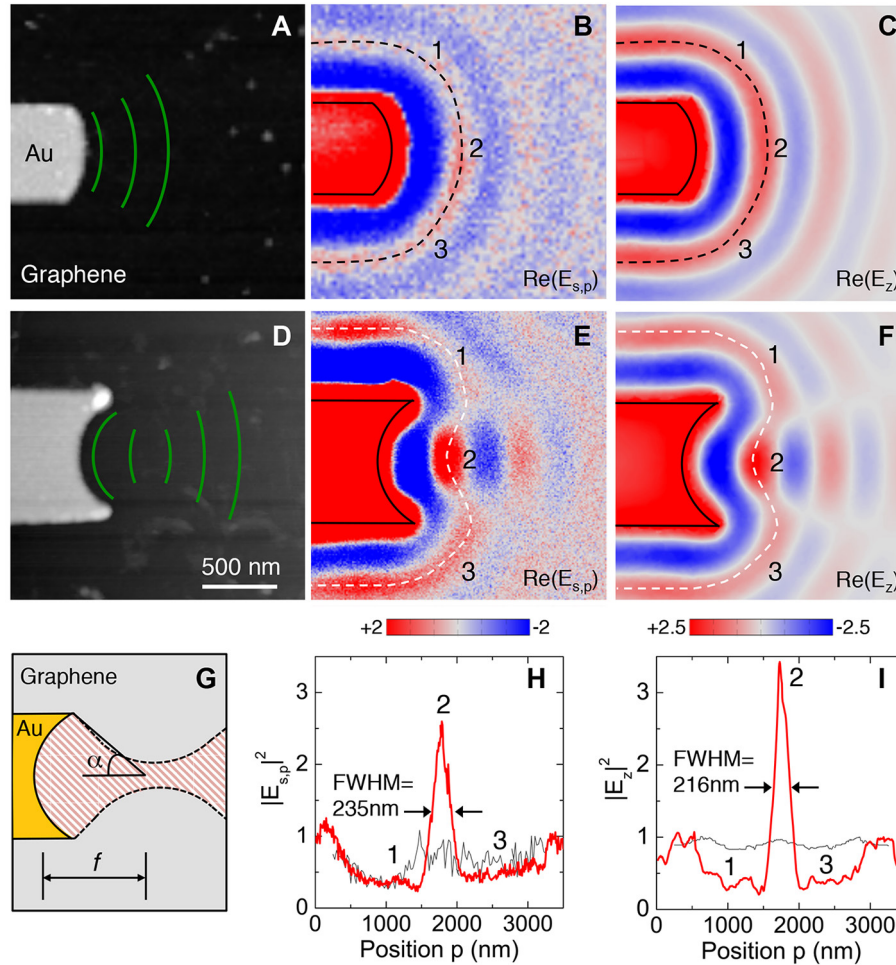
Fig. 3. Wavefront engineering of GPs. (**A** and **D**) Topography, (**B** and **E**) experimental and (**C** and **F**) calculated near-field images, Re($E_{s,p}$) and Re(E_z), of a convex and a concave antenna extremity, respectively ($\lambda_0 = 11.06$ μm). The green lines in the topography images illustrate the GP wavefronts. (**G**) Illustration of GP focusing with a concave antenna extremity. (**H** and **I**) Experimental and calculated near-field intensity (red curves) along the white dashed lines in (E) and (F), respectively. The grey curves show the experimental and calculated near-field intensity along the black dashed lines in (B) and (C), respectively. All curves are normalized to their maximum in the lower left corners of (E) and (F).
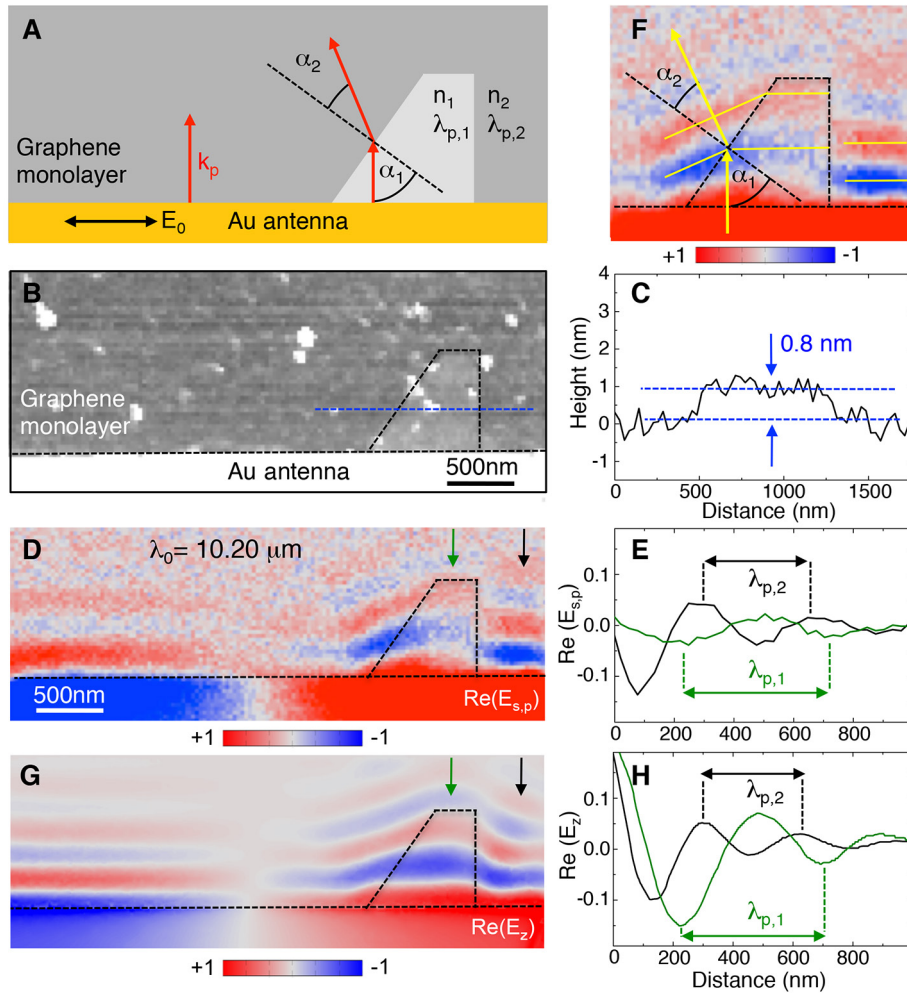
Fig. 4. Refraction of GPs at a graphene bilayer prism. (**A**) Illustration of our experiment and Snell's law of refraction. (**B**) Topography image of a graphene bilayer prism next to a resonant Au antenna. (**C**) Height profile along the dashed blue line in Fig. 3B. (**D**) Near-field image, $Re(E_{s,p})$, recorded simultaneously with the topography shown in Fig. 4B. (**E**) Near-field profiles taken at the positions marked by black and green arrows in (D). (**F**) Analysis of the GP wavefronts. Image extracted from Fig. 4D. (**G**) Calculated near-field image, $Re(E_z)$. (**H**) Near-field profiles taken at the positions marked by black and green arrows in (G).